



Research article

Automatic tooth periodontal ligament segmentation of cone beam computed tomography based on instance segmentation network

Sha Su¹, Xueting Jia¹, Liping Zhan, Siyuan Gao, Qing Zhang, Xiaofeng Huang^{*}

Department of Stomatology, Beijing Friendship Hospital, Capital Medical University, Beijing, China

ARTICLE INFO

Keywords:

Periodontal ligament (PDL)
Deep learning (DL)
Cone-beam computed tomography (CBCT)
Convolutional neural networks (CNNs)
Instance segmentation
Mask R-CNN

ABSTRACT

Objective: The three-dimensional morphological structures of periodontal ligaments (PDLs) are important data for periodontal, orthodontic, prosthodontic, and implant interventions. This study aimed to employ a deep learning (DL) algorithm to segment the PDL automatically in cone-beam computed tomography (CBCT).

Method: This was a retrospective study. We randomly selected 389 patients and 1734 axial CBCT images from the CBCT database, and designed a fully automatic PDL segmentation computer-aided model based on instance segmentation Mask R-CNN network. The labels of the model training were 'teeth' and 'alveolar bone', and the 'PDL' is defined as the region where the 'teeth' and 'alveolar bone' overlap. The model's segmentation performance was evaluated using CBCT data from eight patients outside the database.

Results: Qualitative evaluation indicates that the PDL segmentation accuracy of incisors, canines, premolars, wisdom teeth, and implants reached 100%. The segmentation accuracy of molars was 96.4%. Quantitative evaluation indicates that the mIoU and mDSC of PDL segmentation were $0.667 \pm 0.015 (>0.6)$ and $0.799 \pm 0.015 (>0.7)$ respectively.

Conclusion: This study analysed a unique approach to AI-driven automatic segmentation of PDLs on CBCT imaging, possibly enabling chair-side measurements of PDLs to facilitate periodontists, orthodontists, prosthodontists, and implantologists in more efficient and accurate diagnosis and treatment planning.

1. Introduction

The periodontal ligament (PDL), a distinct connective tissue that attaches between the tooth roots and the inner walls of the alveolar bone socket, is a crucial determinant for making informed decisions regarding dental treatment [1,2]. Morphological changes in the PDL serve as an essential indicator for assessing the severity of periodontal and peri-implant diseases [3]. In addition, PDLs function as dynamic units that undergo reshaping during orthodontic tooth movement [4]. In accordance with Ante's law, evaluating the PDL surface area of the abutment is typically necessary when considering a fixed denture to restore a missing tooth [5]. Therefore, accurate segmentation of a three-dimensional PDL is imperative for effectively planning periodontal, orthodontic, prosthodontic, and implant interventions [6–9].

^{*} Corresponding author. Department of Stomatology, Beijing Friendship Hospital, Capital Medical University, 95 Yong'an Road, Xicheng District, Beijing, 100050, China.

E-mail addresses: huangxf1998@163.com, xiaofengh@ccmu.edu.cn (X. Huang).

¹ These authors contributed equally to this study.

<https://doi.org/10.1016/j.heliyon.2024.e24097>

Received 19 July 2023; Received in revised form 18 December 2023; Accepted 3 January 2024

Available online 9 January 2024

2405-8440/© 2024 Published by Elsevier Ltd.

This is an open access article under the CC BY-NC-ND license

(<http://creativecommons.org/licenses/by-nc-nd/4.0/>).

Previous linear assessment of periodontal attachment loss using periodontal probing may lead to potential overestimation or underestimation of the remaining PDL area [10,11]. The conventional approach include the membrane technique and weight conversion for quantifying the root surface area in vitro fails to capture the PDL's dimensions accurately in vivo [12,13]. In the past 20 years, cone-beam computed tomography (CBCT) combined with 3D reconstruction software such as 3-matic and Mimics has replaced traditional root geometric measurement methods [14]. Many systematic reviews support using CBCT to detect alveolar bone loss [15–17], especially root bifurcation lesions [18]. The high accuracy of CBCT has been demonstrated in numerous studies assessing geometric objects [19,20], teeth [14,21–23], and alveolar bone defects [24].

Currently, segmentation of PDL structures is challenging and laborious without clinically applied systems. Irrespective of purely manual or semi-automatic segmentation procedures, the structure of interest needs to be depicted by human observation [25]. This requirement leads to subjective evaluations made by different inspectors [26,27] and can result in observer fatigue, affecting the technique's reliability [28]. Over the past decade, segmentation methods based on manually defined features, including level sets, graphic cuts, and template fitting, have been investigated extensively [29–31]. Gao et al. [32] proposed an enhanced two-dimensional level set layered model that uses shape and intensity priors to segment tooth roots in the alveolar bone. However, these methods require complex manual initial intervention and corrections; further, they exhibit limited learning, high sensitivity to noise and complex cases, and low robustness when dealing with clinical environments.

In recent years, deep learning (DL) based on convolutional neural networks (CNNs), has gained widespread adoption in detecting, diagnosing, and classifying medical images owing to its exceptional image-processing capabilities [33,34]. CNNs, which are a particular type of machine learning models, are trained with data that is provided in form of pairs of imagery data and a corresponding outcome for the image [35]. Over the past five years, networks based on image classification [36,37], object detection [38,39], semantic segmentation [40–43], and instance segmentation [44] have excelled in the dental field [45]. Although a considerable amount of literature is dedicated to automatic recognition and segmentation of tooth position, research on PDL segmentation is limited [46, 47]. Lee et al. [48] attempted to provide information about alveolar bone loss in two-dimensional radiographs. Li et al. [49] and Gao et al. [32] explored different approaches for automated tooth root segmentation, including a U-Net neural network and improved level set method; however, clear differentiation between tooth root structures and the PDL was not achieved.

Therefore, this study aimed to employ the advanced Mask R-CNN deep learning network for automated segmentation of PDL structures in CBCT images. When a patient undergoes CBCT imaging, direct 3D measurement of the PDL for each tooth is enabled, facilitating chair-side diagnosis and treatment planning for periodontists, orthodontists, prosthodontists, and implantologists.

2. Materials and methods

The processing flowchart of the methodology is shown in Fig. 1.

2.1. Data acquisition for the segmentation model

We randomly selected CBCT image data from the outpatient database of Beijing Friendship Hospital affiliated with Capital Medical University, covering 389 patients between January and September 2022. The patient cohort comprised 205 males and 184 females aged 18–78 years (median age: 26.0 years).

CBCT images were acquired from a CBCT scanner (NewTom CT, Cefla QR Verona; Verona, Italy) with a viewing field of $12 \times 8 \text{ cm}^2$, voxel spacing of 0.3 mm (an isotropic voxel size of 0.3 mm), exposure parameters of 110 kV, 2.1–4.4 mA (depending on subject size),

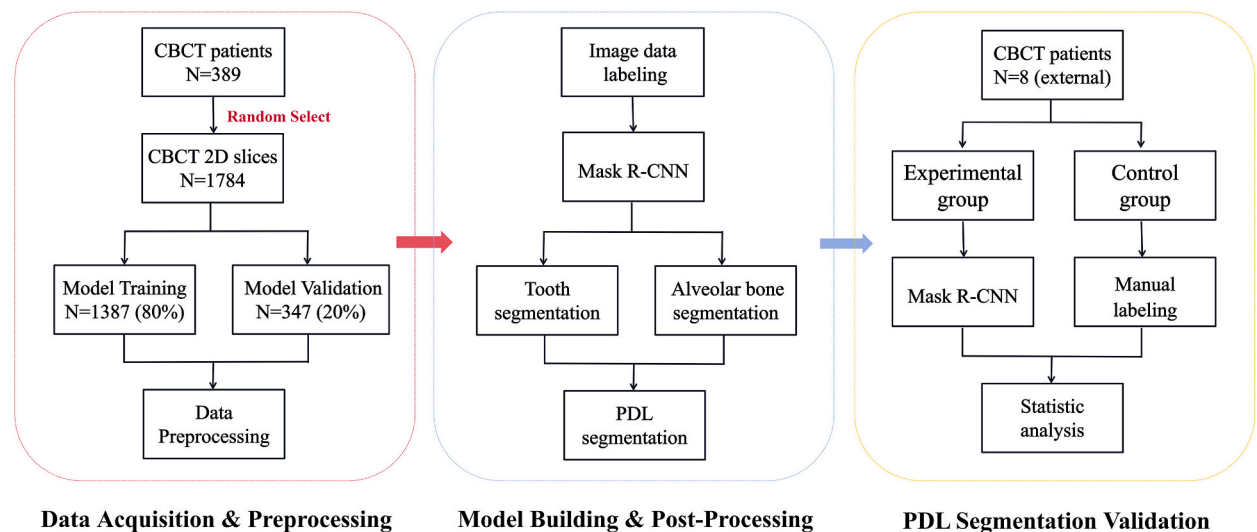


Fig. 1. The entire framework for the PDL segmentation methodology.

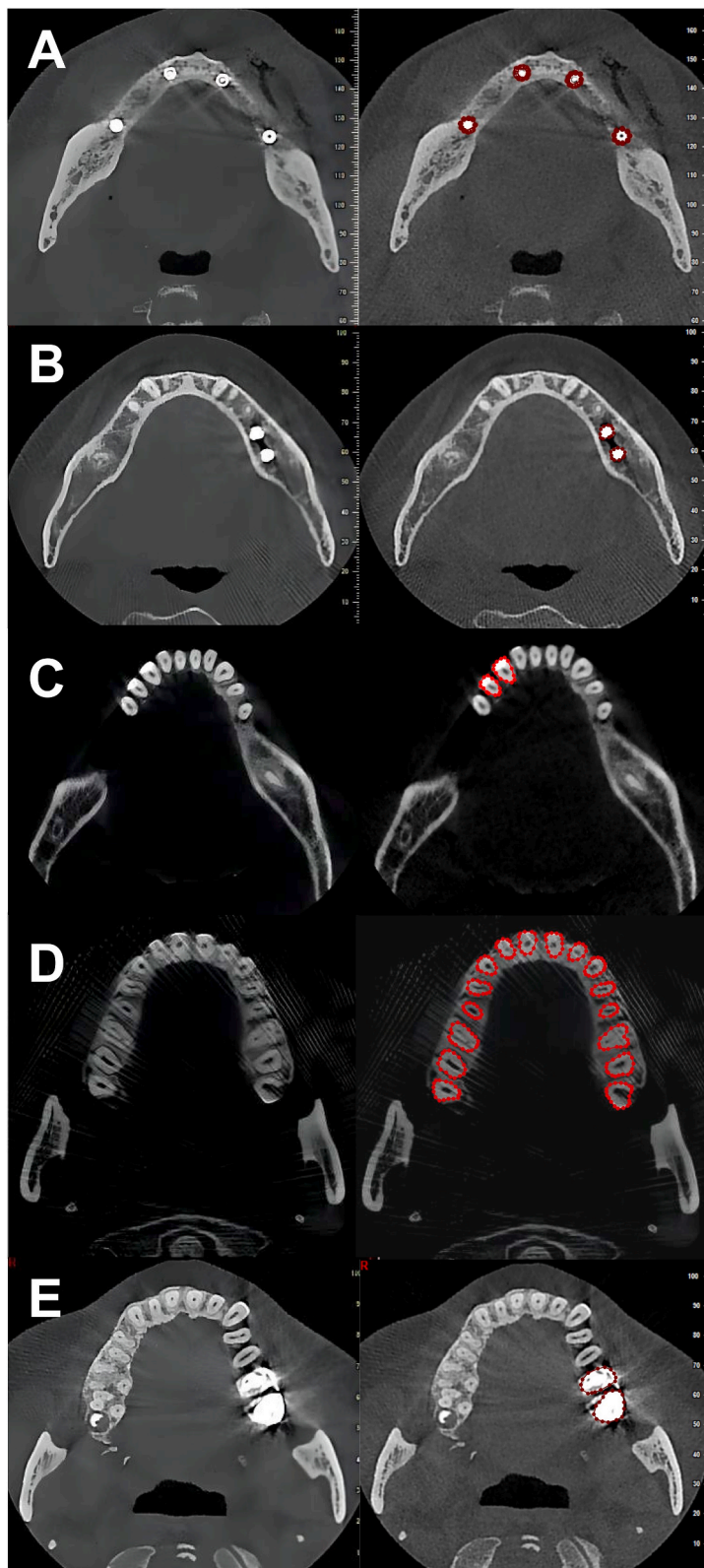


Fig. 2. This diagram illustrates the images and labelling of the various artefacts we included, encompassing implants (A and B), silver–mercury filling body (C), artefact generated by metal and movement around the maxillofacial region (D), and metal crown (E).

and 3.6 s. CBCT scanning was rotated 360°. The 2D images were obtained by reformatting them along the plane perpendicular to those of the axial (or tilted) slice. The output CBCT images and their corresponding parameters were stored in the Digital Imaging and Communications in Medicine (DICOM) file format which is an international standard that defines a format for storing medical images for further analysis [50].

Cases of image blurring caused by artefacts, fillings, metal posts, and head rotation and displacement were included [Fig. 2(A–E)]. A composite of 1734 2D images, ranging from maxillary to mandibular levels, was generated by selecting 4–5 images randomly from the DICOM data of each patient; 80% (1387) of the data was allocated for model training; the remaining 20% (347) was allocated for model validation.

2.2. Data pre-processing

The clinical dental data collected comprises 16-bit CBCT images, necessitating conversion to 24-bit RGB images using computer vision algorithms. The initial step involves establishing a threshold of 6000, followed by truncating and uniformly assigning all CBCT image pixels that surpass this value. Subsequently, the pixels of each CBCT slice image are normalized to a range of 0–255, resulting in an 8-bit grayscale map. Finally, three duplicates of the grayscale image are merged onto the channels to generate a 24-bit RGB image.

2.3. Data labeling

The doctors who participated in the labelling included an attending physician with 5 years of experience, an imaging technician with 7 years of experience, and an associate chief physician with 10 years of experience. We utilized LabelMe (version 3.6; MIT, Computer Science and Artificial Intelligence Laboratory, USA), an open-source annotation tool, to manually label the edges of the teeth and the margins of the upper and lower alveolar bone on 2D images [Fig. 3A, B]. After completing the labelling, we identified areas where alveolar bone overlaps with teeth as the ‘PDL’. Through thorough discussion and double verification, we ensure the utmost accuracy in labeling such intricate images.

2.4. Segmentation model building and post-processing

This study employed a CNN to detect the ‘alveolar bone’ and ‘tooth’ regions automatically in CBCT images. We formulated this task as an instance segmentation problem and utilized the advanced Mask R-CNN [44] for its solution. As our CNN backbone, we adopted ResNet-50 [51], a widely used image classification network in the field of computer vision. Parameters pre-trained on ImageNet (Deng et al., 2009) were used to initialize the model, which was subsequently trained for 12 epochs using an NVIDIA Tesla P100 GPU. The entire training took approximately 1.5 h. An overview of our implemented Mask R-CNN framework can be seen in Fig. 4.

After segmenting the teeth and alveolar bone in the model, we identified the ‘PDL’ region. Each tooth was depicted as a connected component in 3D space. The surface region was made up of edge pixels within the connected component. The edge pixel was classified as a ‘PDL’ pixel if at least one of the eight adjacent pixels in a 2D image belonged to the ‘alveolar bone’ category.

2.5. PDL segmentation results

CBCT images of 8 patients were randomly selected from a database that did not include labelled patients. The CBCT workstation and data processing method remain consistent with the aforementioned description. In the experimental group, the established PDL segmentation model was employed to identify the ‘PDL’ region in each 2D image, and the recognition results of all images were integrated to obtain 3D-level recognition outcomes. Due to segmentation errors, counting connected blocks in the bone’s tooth region resulted in noise points. To address this issue, we comprehensively counted the connected blocks in all PDL regions and implemented a

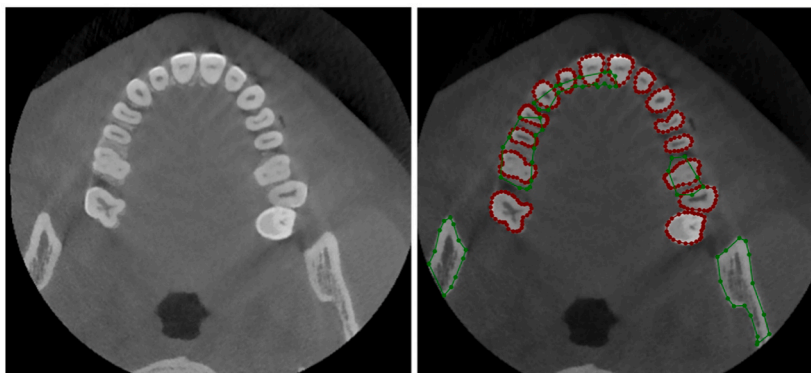


Fig. 3. The labelling process is illustrated in a schematic diagram. One of the original 2D CBCT images is shown with the corresponding labelled image. Green markings indicate the alveolar bone; red markings indicate tooth.

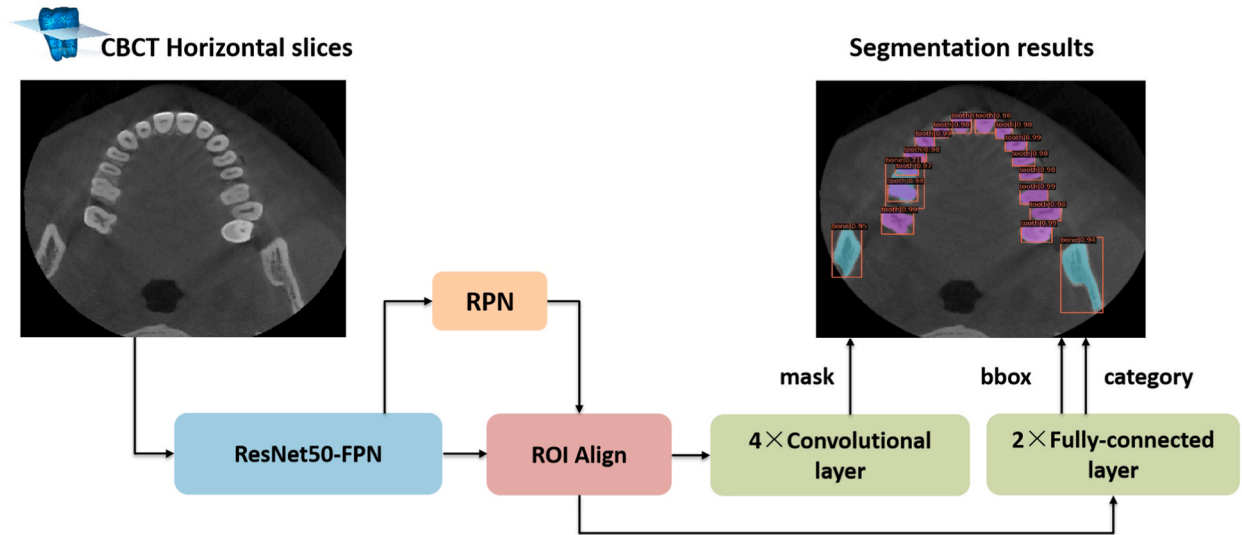


Fig. 4. Overview of the Mask R-CNN [44] framework. The input image is first fed into a ResNet-50 [51] backbone using a feature pyramid network (FPN) [41] to extract the image feature. The Region Proposal Network (RPN) [39] takes image features as input and generates region proposals. The region proposals and the image feature are fed into the region of interest (ROI) Align [44] layer to produce fixed-sized region features. The region features are further used to predict the category, bounding box offset, and binary category mask of the region proposals.

volume threshold (set at 1000 in our experiment) to filter out any connected blocks with volumes below this threshold, thereby retaining only the remaining areas. In the control group, the ground truth for the ‘PDL’ region of each tooth on every 2D image was labelled manually (Fig. 5).

2.6. Evaluation metrics for segmentation

A voxel-wise comparison was used to compare the predictions of the AI segmentation model with the ground truth based on four variables: true positives (TPs), true negatives (TNs), false positives (FPs), and false negatives (FNs). TPs are the correctly segmented voxels of a PDL, while TNs are the correctly not-segmented voxels. FPs are incorrectly segmented voxels, and FNs are missed from segmentation voxels. The following metrics were used for segmentation evaluation:

(1) The intersection over union (IoU) [52] is the number of voxels overlapping between the predicted model and the ground truth. An IoU > 0.6 indicates that the model attained a satisfactory level of training effectiveness [47].

$$IoU = \frac{TP}{TP + FP + FN}$$

(2) The dice similarity coefficient (DSC) [53,54] measures the similarity between the segmented region and the ground truth. DSC > 0.700 indicates a statistically significant overlap effect.

$$DSC = \frac{2 * TP}{2 * TP + FP + FN} = \frac{2 * IoU}{1 + IoU}$$

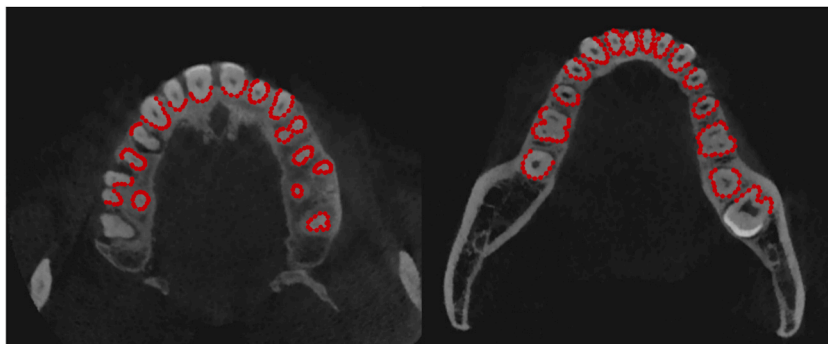


Fig. 5. The red markings indicate the PDL structure. The left image indicates the maxilla; the right image indicates the mandible.

3. Result

3.1. 2D visualization of model segmentation results

The visualization results of tooth and alveolar bone segmentation in CBCT images, based on the Mask R-CNN segmentation model, are presented in Fig. 6. The region where the tooth and alveolar bone intersect corresponds to the “PDL” area.

3.2. 3D visualization of PDL segmentation results

The 3D visualization of the segmentation and reconstruction outcomes of the patient’s PDL is depicted in Fig. 7(A–E). We selected five representative cases to evaluate the performance of our PDL segmentation model. Fig. 7A shows a 2D image of a four-walled osseous defect surrounding the right maxillary second molar. The alveolar bone is absorbed up to 1/3 apical of the tooth root. In the 3D visualization image, the PDL of the right maxillary second molar is shown to be significantly shorter than its root length. Fig. 7B indicates the accuracy segmentation of a mesio-impacted wisdom tooth in the left mandible that deviates from normal dental alignment. Fig. 7C indicates the well performance when alveolar bone resorption extends below the molar bifurcation. The 3D visualization images indicate that the multiple roots of the tooth are independent and cannot be connected automatically. Fig. 7D indicates the segmentation accuracy when alveolar bone resorption is beneath the molar bifurcation. Multiple roots of molars and premolars can be segmented and automatically connected and identified as a unified entity. Fig. 7E indicates the accuracy segmentation of three implants in the posterior mandible.

3.3. Qualitative evaluation of model segmentation performance

Table 1 shows the PDL segmentation results of different types of teeth. The segmentation accuracy of incisors, canines, premolars, wisdom teeth, and implants reached 100%. The segmentation accuracy of molars was 96.4%. The segmentation of two of the seven molars in Patient 6 was found to be inaccurate, as highlighted in bold font. Further, the proximity of the distal buccal root of the patient’s right maxillary first molar to the mesial buccal root of the patient’s right maxillary second molar resulted in incorrect connection and segmentation [Fig. 8(A–C)]. Among the eight patients enrolled in the randomized trials, patient No. 3’s CBCT images exhibited artefacts and slight blurring attributed to metallic interference and patient motion. The segmentation results, however, demonstrate robust performance unaffected by blurring or artefacts. In Patient 7, an additional misclassification occurred where the mandibular alveolar bone dysplasia image was identified erroneously as a PDL structure (Fig. 9).

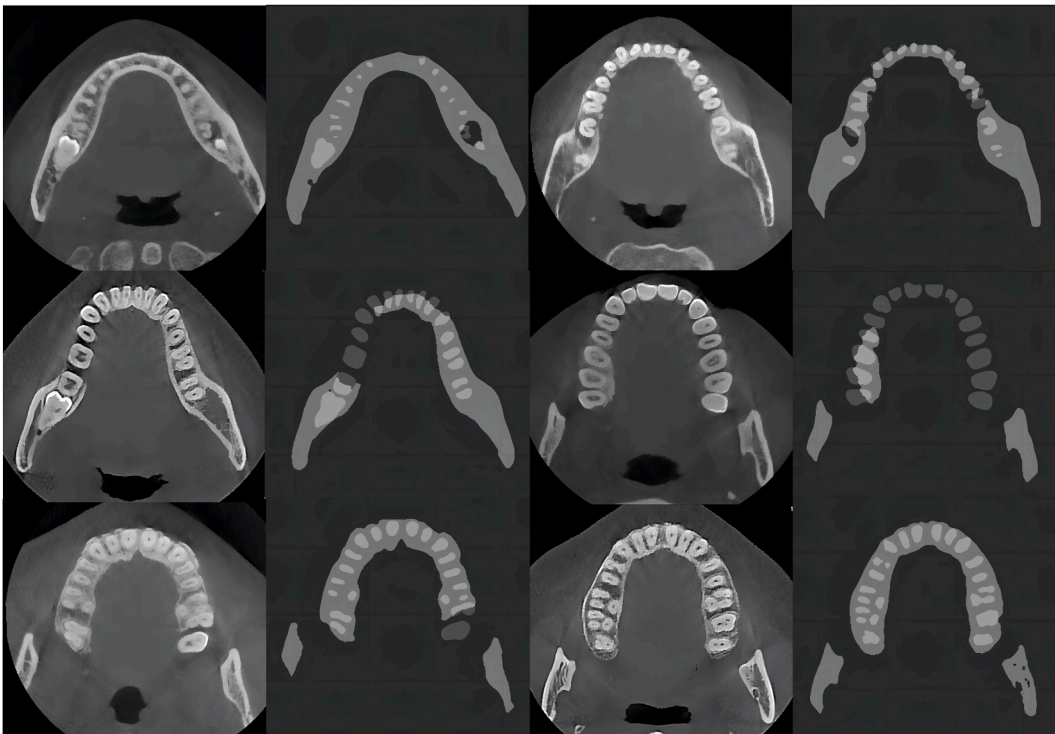


Fig. 6. 2D visualization of tooth and alveolar bone segmentation using distinct coaxial bits as representatives. Dark grey represents the teeth; light grey represents the alveolar bone. The highlighted area where the tooth and alveolar bone overlap is the PDL.

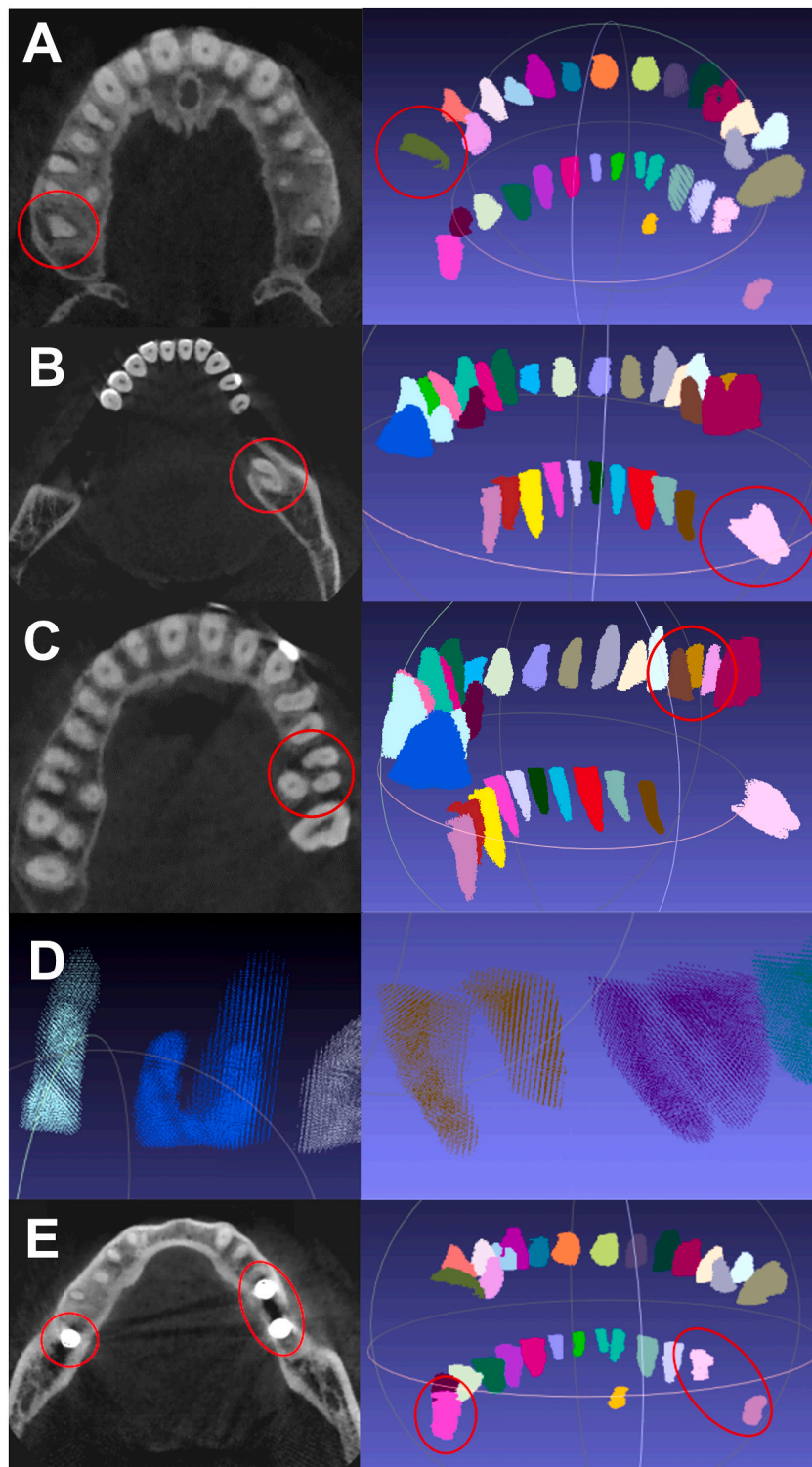


Fig. 7. 3D visualization of the PDL segmentation results. The 2D images of patients are displayed on the left; the PDL segmentation and reconstruction visual images are displayed on the right. A) Maxillary molar with severe alveolar bone resorption. B) mesio-impacted wisdom teeth. C) Alveolar bone absorption below the molar root bifurcation. D) Alveolar bone absorption beneath the molar root bifurcation. E) Implant. Red circles show the positions of representative teeth or implants.

Table 1
Tooth segmentation and segmentation accuracy rates (unit: %).

Patients	AI/Control (Number)						Additional error
	Incisor	Canine	Premolar	Molar	Wisdom tooth	Implant	
1	8/8	4/4	8/8	8/8	2/2	0	0
2	8/8	4/4	8/8	4/4	2/2	0	0
3 ^a	8/8	4/4	8/8	8/8	3/3	0	0
4	8/8	4/4	8/8	8/8	4/4	0	0
5	7/7	4/4	8/8	8/8	4/4	0	0
6	7/7	4/4	8/8	5/7	4/4	0	0
7	8/8	4/4	8/8	5/5	0/0	3/3	1
8	8/8	4/4	8/8	8/8	4/4	0	0
Accuracy rate (%)	100	100	100	96.4	100	100	

^a The CBCT image of this patient exhibits mild motion-related artefacts.

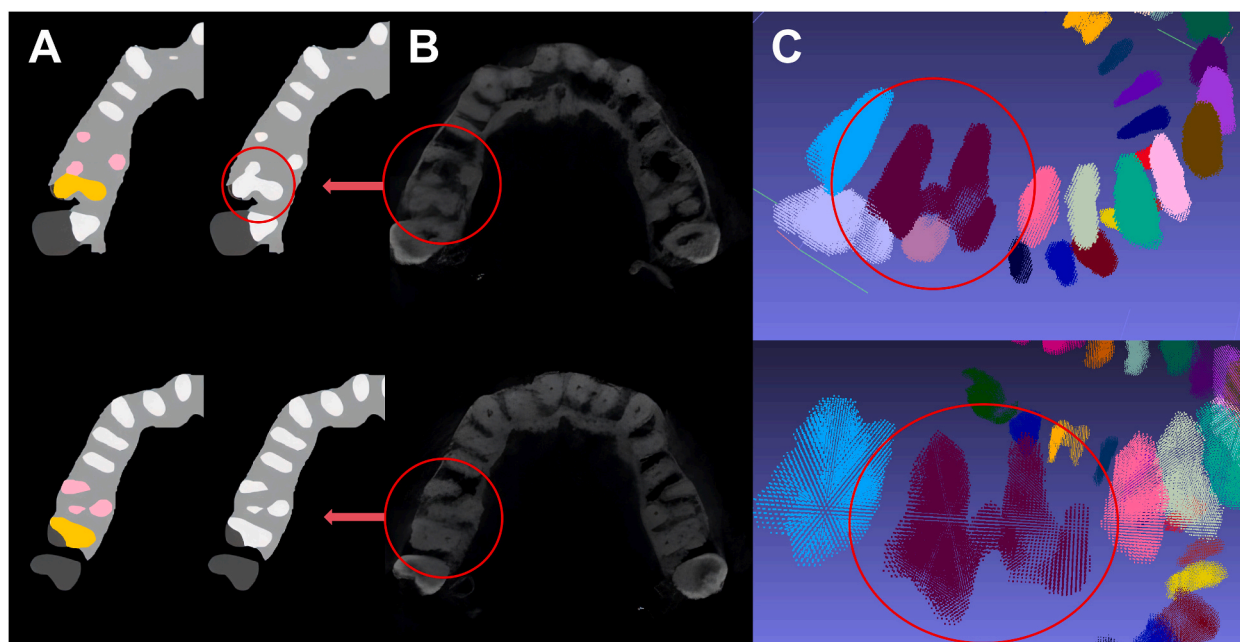


Fig. 8. The diagram illustrates the segmentation error observed in the 2 M. A) The model segmentation visualization: the pink region represents the three roots of the patient's right maxillary first molar; the yellow region represents the patient's right maxillary second molar. The red circle indicates an erroneous segmentation of the roots of two teeth into a single root. B) The unaltered original 2D image: the red circle indicates the precise location of the patient's two maxillary molars of different axial levels. C) Visualization of the PDL 3D segmentation results: the red circle indicates that the two maxillary molars were incorrectly interconnected and integrated with the same colour.

3.4. Quantitative evaluation of model segmentation performance

The mean intersection over union (mIOU) values for tooth, alveolar bone, and PDL were 0.894, 0.836, and 0.667, respectively. The mean dice similarity coefficient (DSC) values for tooth, alveolar bone, and PDL were 0.934, 0.908, and 0.799, respectively. The mIOU values for alveolar bone, tooth, and PDL exceeded 0.6; the mDSC surpassed 0.7 (Table 2).

4. Discussion

In this study, we designed a tooth, alveolar bone, and PDL segmentation network based on the advanced Mask R-CNN, and devised an ingenious PDL segmentation methodology. By segmenting the boundaries between teeth and alveolar bone precisely, the overlapping region of each tooth and alveolar bone was identified as the PDL area. The qualitative assessment showed that the PDL segmentation accuracy of the incisor, canine, premolar, wisdom tooth, and implant achieved a perfect score of 100%; molars exhibited a 96.4% accuracy rate. The mDSC values for tooth, alveolar bone, and PDL were 0.934, 0.908, and 0.799, respectively.

The results demonstrate that the model exhibits excellent segmentation performance in tooth and alveolar bone, achieving high mDSC values of 0.934 and 0.908. Numerous prior studies have employed diverse 2D or 3D deep learning networks for teeth

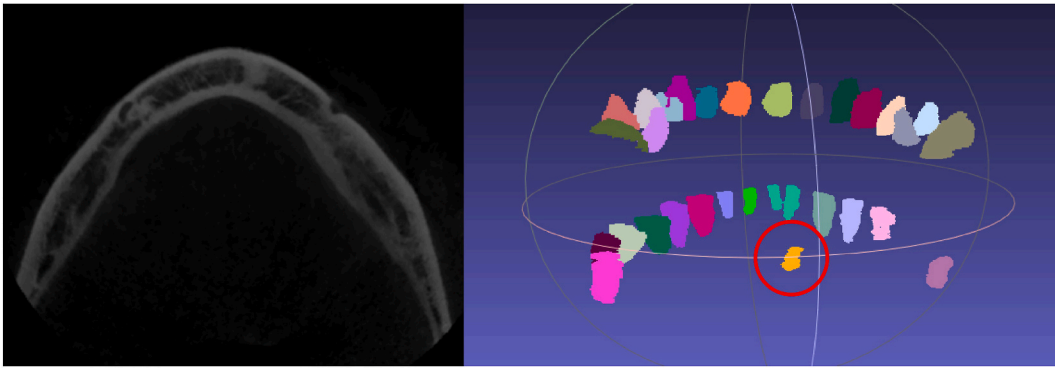


Fig. 9. The red circle in the left image highlights an alveolar bone dysplasia structure located in the anterior region of the mandible. In the right image, this structure is misclassified as a PDL structure.

Table 2

Evaluation of alveolar bone, tooth, and PDL segmentation performance.

Segmentation	mIoU	mDSC
Air	0.990 ± 0.008	0.995 ± 0.004
Tooth	0.894 ± 0.017	0.934 ± 0.005
Alveolar bone	0.836 ± 0.020	0.908 ± 0.032
PDL	0.667 ± 0.015	0.799 ± 0.015

mIoU: mean intersection over union; mDSC: mean dice similarity coefficient.

segmentation, yielding DSC ranging from 0.880 to 0.962. Wu et al. [55] (2020) proposed a 3D neural network called GH + BAD-ice-DenseASPP-UNet + LO for tooth segmentation, which currently achieves the highest precision in tooth segmentation with a Dice similarity coefficient (DSC) of 0.962. Similar to our study, Wang et al. [56] (2021) employed a 2D neural network called MS-D to systematically segment teeth and alveolar bone, yielding an impressive mDSC of 0.934 for teeth and 0.945 for alveolar bone.

However, empirical research on the segmentation network for PDLs is scarce. Li et al. [49] constructed the AttU-Net + BDC lstm network to segment the “tooth root” in CBCT images; DSC reached 0.955. This study categorized all teeth into roots based on a common horizontal plane. However, upon examining the labelling diagram of the model training, it became evident that such an approach for selecting root segments was inappropriate. The study, however, failed to distinguish between the root and PDL as distinct structures accurately. The PDL differs from the root structure; its dimensions vary with the extent of alveolar bone resorption over an individual’s lifespan. Inflammation of periodontal tissue, such as from chronic periodontitis or traumatic stimulation like occlusal trauma, results in complications, including gingival recession, alveolar bone resorption, and diminished bone support and mechanical stress resistance, ultimately leading to tooth mobility and potential loss [3]. The simple surface area of the root cannot serve as a representative measure for the PDL.

In addition, segmenting the tooth’s PDL is a challenge in CBCT image segmentation. Since the PDL’s thickness typically measures 0.15–0.38 mm [57], it is often indiscernible in CBCT images, resulting in blurred edges [29]. The cementum and alveolar bone of teeth have similar threshold values; owing to their comparable densities, differentiating the root from the alveolar bone by adjusting the grey threshold range is not feasible.

In this study, the mIoU and DSC values for PDLs were 0.667 and 0.799, respectively. The PDL segmentation accuracy was not as good as that of teeth and alveolar bone. This may have been due to the following reasons: (1) the overlap of the girth model poses a greater challenge than that of the cross-sectional model. Each horizontal two-dimensional section identifies a circle within the “PDL” corresponding to the ellipse’s perimeter rather than its cross-sectional area. Therefore, the model’s task is to accurately segment 2D lines, posing challenges in achieving a significantly high level of segmentation accuracy; (2) the accuracy of PDL segmentation is influenced by the segmentation accuracy of teeth and alveolar bone, thereby leading to an increase in segmentation error; (3) labelling PDLs accurately is a challenging task for clinicians with expertise. Linear marking necessitates greater precision compared to frame and circle marking, consequently diminishing the accuracy of the ground-truth value itself.

However, the IoU score serves as a standardized performance metric for object class segmentation problems, and the model undergoes rigorous evaluation, with even minor discrepancies in pixel values being deemed inadequate. Therefore, a value >0.6 indicates the model achieved a satisfactory level of training effectiveness [47]. The voxel-wise matching accuracy of each label was computed by a similar DSC, which evaluated the degree of overlap between algorithmic segmentation and manual segmentation. A DSC score >0.7 indicates a significant level of overlap effect [52]. Therefore, the segmentation model of PDL is acceptable.

The database cohort in this study comprised a diverse range of complex data, including impacted teeth, metal restorations, and implants, as well as instances where the image data was blurred due to motion artefacts. The aim is to enhance the network’s generalization and robustness, thereby improving its practical applicability. The test model demonstrated robust performance,

successfully segmenting complex case scenarios in the eight test patients, including impacted wisdom teeth, implants, and cases affected by artefacts. In the future, this model can provide valuable data for studying impacted wisdom teeth and peri-implant inflammation. In addition, the study segmented the root portion located within the alveolar bone, minimizing the effect of the metal crown on the results and thereby enhancing the network's practicality.

The segmentation errors identified in this study included misclassifying mandibular bone dysplasia as "dental" structures. This error may be attributed to including complex cases of heterotopic impacted teeth in the study's learning labelling samples, resulting in the misidentification of high-density images in unconventional dentition as "tooth" structures. However, oral clinicians can easily identify and correct this segmentation error through manual post-processing.

In the qualitative analysis of the eight patients, one patient was found to have segmentation errors caused by the connection between the two adjacent molar teeth on the upper right side. Such cases are common due to the root and apical area proximity. Therefore, addressing this challenge becomes crucial in our study, since we aim to enhance PDL segmentation accuracy with a more advanced 3D segmentation network in the future.

Another limitation of this study is that the method is new, although the qualitative and quantitative analysis of eight patients verified the accuracy of the results. Increasing the reliability of the PDL results obtained by radiographic segmentation and pixel counting requires more diverse data and greater sample sizes. Each patient may have a different configuration; thus, anatomical variation can also constrain calculations. Therefore, in the future, we will continue to expand the sample size of patient measurements and add quantitative data from real PDL areas for comparative validation.

5. Conclusion

This study presents a novel AI-driven approach for automatically segmenting the PDL on CBCT imaging, laying the foundation for future deep-learning models to calculate the PDL area or volume directly in CBCT 3D images. The research team aims to further enhance and develop the PDL segmentation system, facilitating more efficient and accurate diagnosis and treatment planning for periodontists, orthodontists, prosthodontists, and implantologists.

Ethics declarations

This study was reviewed and approved by the Research Ethics Committee of the Beijing Friendship Hospital, Capital Medical University (approval number: 2021-P-130-01) and conducted in accordance with the principles of the Declaration of Helsinki. Informed consent was not required for this study because 1) The image data used in this study were obtained from routine clinical diagnosis and treatment; 2) Waiving informed consent will not adversely affect the rights and health of the subjects; 3) The personal information of the subjects will be strictly protected; 4) The risk to the subjects in this study is no greater than minimal risk; 5) Conducting the study would be impossible if informed consent were required; 6) The research project does not involve personal privacy or commercial interests.

Data availability statement

The codes used for pre-processing and deep learning include proprietary parts and cannot be released publicly to protect the privacy of individuals who participated in the study. However, the pre-processing, deep learning algorithms, and data generated or analysed during this study are included in this published article and its supplementary information files. The datasets used and/or analysed during the current study are available from the corresponding author upon reasonable request.

CRedit authorship contribution statement

Sha Su: Writing - review & editing, Writing - original draft, Formal analysis, Conceptualization. **Xueting Jia:** Methodology. **Liping Zhan:** Writing - original draft, Formal analysis. **Siyuan Gao:** Writing - original draft, Methodology. **Qing Zhang:** Software, Methodology, Formal analysis. **Xiaofeng Huang:** Funding acquisition, Conceptualization.

Declaration of competing interest

The authors declare the following financial interests/personal relationships which may be considered as potential competing interests: Xiaofeng Huang reports financial support was provided by This work was supported by Clinical Technology Innovation Project of Beijing Hospital Management Center, China (XMLX202132). Xueting Jia reports financial support was provided by National Natural Science Foundation of China, China (No. 82101005).

Acknowledgements

This work was supported by the Clinical Technology Innovation Project of Beijing Hospital Management Center (XMLX20213; Xiao-feng Huang) and the National Natural Science Foundation of China (No. 82101005; Xueting Jia).

Appendix A. Supplementary data

Supplementary data to this article can be found online at <https://doi.org/10.1016/j.heliyon.2024.e24097>.

References

- [1] S. Hirashima, T. Kanazawa, K. Ohta, K.I. Nakamura, Three-dimensional ultrastructural imaging and quantitative analysis of the periodontal ligament, *Anat. Sci. Int.* 95 (1) (2020) 1–11.
- [2] W. Beertsen, C.A. McCulloch, J. Sodek, The periodontal ligament: a unique, multifunctional connective tissue, *Periodontol* 13 (1997) (2000) 20–40.
- [3] N.P. Lang, P.M. Bartold, Periodontal health, *J. Periodontol.* 89 (Suppl 1) (2018) S9–S16.
- [4] Y. Li, L.A. Jacox, S.H. Little, C.C. Ko, Orthodontic tooth movement: the biology and clinical implications, *Kaohsiung J. Med. Sci.* 34 (4) (2018) 207–214.
- [5] M. Lulic, U. Brägger, N.P. Lang, M. Zwahlen, G.E. Salvi, Ante's (1926) law revisited: a systematic review on survival rates and complications of fixed dental prostheses (FDPs) on severely reduced periodontal tissue support, *Clin. Oral Implants Res.* 18 (Suppl 3) (2007) 63–72.
- [6] B.K. Berkovitz, The structure of the periodontal ligament: an update, *Eur. J. Orthod.* 12 (1) (1990) 51–76.
- [7] S.B. Park, S.Y. An, W.J. Han, J.T. Park, Three-dimensional measurement of periodontal surface area for quantifying inflammatory burden, *J. Periodontol. Implant. Sci.* 47 (3) (2017) 154–164.
- [8] M.K. McGuire, M.E. Nunn, Prognosis versus actual outcome. II. The effectiveness of clinical parameters in developing an accurate prognosis, *J. Periodontol.* 67 (7) (1996) 658–665.
- [9] M.K. McGuire, M.E. Nunn, Prognosis versus actual outcome. III. The effectiveness of clinical parameters in accurately predicting tooth survival, *J. Periodontol.* 67 (7) (1996) 666–674.
- [10] K.S. Klock, N.R. Gjerdet, O. Haugejorden, Periodontal attachment loss assessed by linear and area measurements in vitro, *J. Clin. Periodontol.* 20 (6) (1993) 443–447.
- [11] S.K. Chen, J.H. Pan, C.M. Chen, J.Y. Jeng, Accuracy of supported root ratio estimation from projected length and area using digital radiographs, *J. Periodontol.* 75 (6) (2004) 866–871.
- [12] J.K. Mowry, M.G. Ching, M.D. Orjansen, C.M. Cobb, L.R. Friesen, S.R. MacNeill, J.W. Rapley, Root surface area of the mandibular cuspid and bicuspid, *J. Periodontol.* 73 (10) (2002) 1095–1100.
- [13] P.P. Huijoe, A meta-analysis of normal ranges for root surface areas of the permanent dentition, *J. Clin. Periodontol.* 21 (4) (1994) 225–229.
- [14] P. Jia, G. Yang, W. Hu, K.H. Chung, Y. Zhao, M. Liu, C.S. Chen, Comparison of in situ cone beam computed tomography scan data with ex vivo optical scan data in the measurement of root surface area, *Oral Surg. Oral Med. Oral Pathol. Oral Radiol.* 128 (5) (2019) 552–557.
- [15] C. Walter, J.C. Schmidt, C.A. Rinne, S. Mendes, K. Dula, A. Sculean, Cone beam computed tomography (CBCT) for diagnosis and treatment planning in periodontology: systematic review update, *Clin. Oral Invest.* 24 (9) (2020) 2943–2958.
- [16] C. Walter, J.C. Schmidt, K. Dula, A. Sculean, Cone beam computed tomography (CBCT) for diagnosis and treatment planning in periodontology: a systematic review, *Quintessence Int. (Berlin, Germany : 1985)* 47 (1) (2016) 25–37.
- [17] G.A. Mandelaris, R. Neiva, L. Chambrone, Cone-beam computed tomography and interdisciplinary dentofacial therapy: an American academy of periodontology best evidence review focusing on risk assessment of the dentoalveolar bone changes influenced by tooth movement, *J. Periodontol.* 88 (10) (2017) 960–977.
- [18] J.P. Woelber, J. Fleiner, J. Rau, P. Ratka-Krüger, C. Hannig, Accuracy and usefulness of CBCT in periodontology: a systematic review of the literature, *Int. J. Periodontics Restor. Dent.* 38 (2) (2018) 289–297.
- [19] H.M. Pinsky, S. Dyda, R.W. Pinsky, K.A. Misch, D.P. Sarment, Accuracy of three-dimensional measurements using cone-beam CT, *Dentomaxillofacial Radiol.* 35 (6) (2006) 410–416.
- [20] C.A. Lascala, J. Panella, M.M. Marques, Analysis of the accuracy of linear measurements obtained by cone beam computed tomography (CBCT-NewTom), *Dentomaxillofacial Radiol.* 33 (5) (2004) 291–294.
- [21] Y.H. Sang, H.C. Hu, S.H. Lu, Y.W. Wu, W.R. Li, Z.H. Tang, Accuracy assessment of three-dimensional surface reconstructions of in vivo teeth from cone-beam computed tomography, *Chin. Med. J.* 129 (12) (2016) 1464–1470.
- [22] H. Lund, Cone beam computed tomography in evaluations of some side effects of orthodontic treatment, *Swed. Dent. J.* (219) (2011) 4–78. Supplement.
- [23] J.F. Sherrard, P.E. Rossow, B.W. Benson, R. Carrillo, P.H. Buschang, Accuracy and reliability of tooth and root lengths measured on cone-beam computed tomographs, *Am. J. Orthod. Dentofacial Orthop.* 137 (4 Suppl) (2010) S100–S108.
- [24] Y.J. Guo, Z.P. Ge, R.H. Ma, J.X. Hou, G. Li, A six-site method for the evaluation of periodontal bone loss in cone-beam CT images, *Dentomaxillofacial Radiol.* 45 (1) (2016) 20150265.
- [25] J. Tasanapanont, J. Apisariyakul, T. Wattanachai, P. Sriwilas, M. Midtbø, D. Jotikasthira, Comparison of 2 root surface area measurement methods: 3-dimensional laser scanning and cone-beam computed tomography, *Imaging Sci. Dent.* 47 (2) (2017) 117–122.
- [26] M. Rana, D. Modrow, J. Keuchel, C. Chui, M. Rana, M. Wagner, N.C. Gellrich, Development and evaluation of an automatic tumor segmentation tool: a comparison between automatic, semi-automatic and manual segmentation of mandibular odontogenic cysts and tumors, *J. Cranio-Maxillo-Fac. Surg.* 43 (3) (2015) 355–359.
- [27] K. Vallaeys, A. Kacem, H. Legoux, M. Le Tenier, C. Hamitouche, R. Arbab-Chirani, 3D dento-maxillary osteolytic lesion and active contour segmentation pilot study in CBCT: semi-automatic vs manual methods, *Dentomaxillofacial Radiol.* 44 (8) (2015) 20150079.
- [28] P.A. Yushkevich, J. Piven, H.C. Hazlett, R.G. Smith, S. Ho, J.C. Gee, G. Gerig, User-guided 3D active contour segmentation of anatomical structures: significantly improved efficiency and reliability, *Neuroimage* 31 (3) (2006) 1116–1128.
- [29] D.X. Ji, S.H. Ong, K.W. Foong, A level-set based approach for anterior teeth segmentation in cone beam computed tomography images, *Comput. Biol. Med.* 50 (2014) 116–128.
- [30] B. Wang, X. Gao, D. Tao, X. Li, A unified tensor level set for image segmentation, *IEEE Trans. Syst. Man Cybern. B Cybern.: Pub. IEEE Syst. Man Cybernet. Soc.* 40 (3) (2010) 857–867.
- [31] S. Barone, A. Paoli, A.V. Rationale, CT segmentation of dental shapes by anatomy-driven reformation imaging and B-spline modelling, *Int. J. Numer. Method Biomed. Eng.* 32 (6) (2016).
- [32] H. Gao, O. Chae, Individual tooth segmentation from CT images using level set method with shape and intensity prior, *Pattern Recogn.* 43 (7) (2010) 2406–2417.
- [33] A. Hosny, C. Parmar, J. Quackenbush, L.H. Schwartz, H. Aerts, Artificial intelligence in radiology, *Nat. Rev. Cancer* 18 (8) (2018) 500–510.
- [34] S. Khan, H. Rahmani, S.A.A. Shah, M. Bennamoun, A guide to convolutional neural networks for computer vision, *Synthesis Lect. Comp. Vision* 8 (1) (2018) 1–207.
- [35] F. Schwendicke, T. Golla, M. Dreher, J. Krois, Convolutional neural networks for dental image diagnostics: a scoping review, *J. Dent.* 91 (2019) 103226.
- [36] A. Krizhevsky, I. Sutskever, G.E. Hinton, ImageNet classification with deep convolutional neural networks, *Adv. Neural Inf. Process. Syst.* 25 (2) (2012).
- [37] S. Xie, R. Girshick, P. Dollár, Z.W. Tu, K.M. He, Aggregated Residual Transformations for Deep Neural Networks, *IEEE*, 2016.
- [38] T.Y. Lin, P. Dollár, R. Girshick, K. He, B. Hariharan, S. Belongie, Feature pyramid networks for object detection, in: *Proceedings of the IEEE Conference on Computer Vision and Pattern Recognition*, 2017, pp. 2117–2125.
- [39] S. Ren, K. He, R. Girshick, J. Sun, R.-C.N.N. Faster, Towards real-time object detection with region proposal networks, *IEEE Trans. Pattern Anal. Mach. Intell.* 39 (6) (2017) 1137–1149.

- [40] E. Shelhamer, J. Long, T. Darrell, Fully convolutional networks for semantic segmentation, *IEEE Trans. Pattern Anal. Mach. Intell.* 39 (4) (2017) 640–651.
- [41] O. Ronneberger, P. Fischer, T. Brox, U-net: Convolutional Networks for Biomedical Image Segmentation, Springer International Publishing, 2015, pp. 234–241.
- [42] F. Milletari, N. Navab, S.A. Ahmadi, V-Net, Fully Convolutional Neural Networks for Volumetric Medical Image Segmentation, *IEEE*, 2016.
- [43] L.C. Chen, G. Papandreou, I. Kokkinos, K. Murphy, A.L. Yuille, DeepLab: semantic image segmentation with deep convolutional nets, atrous convolution, and fully connected CRFs, *IEEE Trans. Pattern Anal. Mach. Intell.* 40 (4) (2018) 834–848.
- [44] K. He, G. Gkioxari, P. Dollar, R. Girshick, Mask R-CNN, *IEEE Trans. Pattern Anal. Mach. Intell.* 42 (2) (2020) 386–397.
- [45] F. Schwendicke, W. Samek, J. Krois, Artificial intelligence in dentistry: chances and challenges, *J. Dent. Res.* 99 (7) (2020) 769–774.
- [46] T.J. Jang, K.C. Kim, H.C. Cho, J.K. Seo, A fully automated method for 3D individual tooth identification and segmentation in dental CBCT, *IEEE Trans. Pattern Anal. Mach. Intell.* 44 (10) (2022) 6562–6568.
- [47] P. Lahoud, M. EzEldeen, T. Beznik, H. Willems, A. Leite, A. Van Gerven, R. Jacobs, Artificial intelligence for fast and accurate 3-dimensional tooth segmentation on cone-beam computed tomography, *J. Endod.* 47 (5) (2021) 827–835.
- [48] C.T. Lee, T. Kabir, J. Nelson, S. Sheng, H.W. Meng, T.E. Van Dyke, M.F. Walji, X. Jiang, S. Shams, Use of the deep learning approach to measure alveolar bone level, *J. Clin. Periodontol.* 49 (3) (2022) 260–269.
- [49] Q. Li, K. Chen, L. Han, Y. Zhuang, J. Li, J. Lin, Automatic tooth roots segmentation of cone beam computed tomography image sequences using U-net and RNN, *J. X Ray Sci. Technol.* 28 (5) (2020) 905–922.
- [50] M. Larobina, Thirty years of the DICOM standard, *Tomography* 9 (5) (2023) 1829–1838.
- [51] K.M. He, X.Y. Zhang, S.Q. Ren, J. Sun, Deep residual learning for image recognition, in: *Proceedings of the IEEE Conference on Computer Vision and Pattern Recognition*, 2016, pp. 770–778.
- [52] A.P. Zijdenbos, B.M. Dawant, R.A. Margolin, A.C. Palmer, Morphometric analysis of white matter lesions in MR images: method and validation, *IEEE Trans. Med. Imag.* 13 (4) (1994) 716–724.
- [53] L.R. Dice, Measures of the amount of ecologic association between species, *Ecology* 26 (3) (1945) pp297–302.
- [54] P.F. Raudaschl, P. Zaffino, G.C. Sharp, et al., Evaluation of segmentation methods on head and neck CT: auto-segmentation challenge 2015, *Med. Phys.* 44 (5) (2017) 2020–2036.
- [55] X.Y. Wu, H. Chen, Y.J. Huang, H.Y. Guo, L.S. Wang, Center-sensitive and boundary-aware tooth instance segmentation and classification from cone-beam CT, in: *2020 IEEE 17th International Symposium on Biomedical Imaging (ISBI)*, 2020, pp. 939–942.
- [56] H. Wang, J. Minnema, K.J. Batenburg, T. Forouzanfar, F.J. Hu, G. Wu, Multiclass CBCT image segmentation for orthodontics with deep learning, *J. Dent. Res.* 100 (9) (2021) 943–949.
- [57] W.J. Ralph, J.R. Jefferies, The minimal width of the periodontal space, *J. Oral Rehabil.* 11 (5) (1984) 415–418.